Facile Synthesis, Characterization, and Visible-light Photocatalytic Activities of 3D Hierarchical Bi$_2$S$_3$ Architectures Assembled by Nanoplatelets

Tiekun Jia [1],*, Xiaofeng Wang [1], Fei Long [2], Jili Li [1], Zhihua Kang [2], Fang Fu [1], Guang Sun [3] and Jian Chen [1]

[1] School of Materials Science and Engineering, Luoyang Institute of Science and Technology, Luoyang 471023, China; wang928199@126.com (X.W.); lijili328@126.com (J.L.); fufang1@126.com (F.F.); chenxiaojian@126.com (J.C.)

[2] School of Materials Science and Engineering, Guilin University of Technology, Guilin 541004, China; longf@glut.edu.cn (F.L); 15236262896@163.com (Z.K.)

[3] School of Materials Science and Engineering, Henan Polytechnic University, Jiaozuo 45400, China; mcsunguang@163.com

* Correspondence: tiekunjia@126.com or tkjia@whut.edu.cn; Tel./Fax: +86-379-6592-8196

Abstract: 3D hierarchical Bi$_2$S$_3$ architectures have been successfully synthesized via a simple and effective hydrothermal process. The as-prepared Bi$_2$S$_3$ samples were characterized by X-ray diffraction (XRD), scanning electron microscopy (SEM), transmission electron microscopy (TEM), nitrogen adsorption- desorption isotherms, and UV-vis diffuse reflectance spectrum (DRS). The observation of field emission scanning electron microscope (FESEM) images showed that numerous nanoplatelets are randomly arranged and interconnected with each other, which are assembled into 3D hierarchical Bi$_2$S$_3$ architectures. The photocatalytic activity of the as-prepared Bi$_2$S$_3$ samples was evaluated by the degradation of Rhodamine B (RhB) under visible light irradiation. The effect of hydrothermal temperature, reaction time, pH value and shape on the photocatalytic efficiency of the as-prepared Bi$_2$S$_3$ samples was investigated. The results showed that 3D hierarchical Bi$_2$S$_3$ architectures prepared at 165 °C for 12 h at a pH of 2.4 exhibits high photocatalytic efficiency, which could be ascribed to the synergetic effect of the shape, surface area, crystallinity, band gap and crystalline size.

Keywords: Bi$_2$S$_3$; hierarchical architectures; hydrothermal synthesis; photocatalytic activities

1. Introduction

Nowadays, we are confronted with the problem related to various organic pollutants releasing from various textile and chemical plants accompanied with the continuously increasing industrialization. Most organic pollutants are difficult to effectively dispose of by natural means, leading to water sources and the environment to be contaminated and polluted. Subsequently, the contaminated water source and the polluted air have become an enormous threat to public health. Photocatalysis, considered an efficient and reliable technology for the environmental remediation of poisonous organic pollutants, has the merits of simple operation, ambient condition, low cost, high efficiency and reusability [1,2]. Over the past decade, TiO$_2$ has been widely investigated as one of the most representative photocatalysts for degrading pollutants. However, traditional TiO$_2$ exhibits ineffective photocatalytic performance under visible light irradiation due to its wide band gap and low quantum efficiency. Therefore, the development of novel visible-light-driven photocatalysts is required for the purpose of taking full use of solar energy and improving quantum efficiency. In order

to achieve the goal, much research has been devoted to the modification of traditional TiO_2 [3–7] and the pursuit of other materials such as bismuth sulfide (Bi_2S_3) [8–10].

With a direct narrow band gap of around 1.3 eV, bismuth sulfide (Bi_2S_3), emerging as one promising member of group V–VI binary semi-conductors, has been attracting considerable attention due to its wide range of application in the field of solar cells [8,9], photo-detectors [10–14], gas sensors [14], thermoelectric devices [15], X-ray computed tomography imaging [16], lithium-ion batteries [17–20], and photocatalysis [21–23]. Bi_2S_3 micro/nanostructures with various morphologies, including one-dimensional (1D) nanorods/nanowires, two-dimensional (2D) nanosheets/flakes, and three-dimensional (3D) hierarchical complex architectures, have been successfully fabricated in previous studies [10–15,17–19,23–26], since the properties of functional nanostructured materials are strongly dependent on the tailored morphology, microstructure and surface properties. Among them, 3D hierarchical complex architectures have exhibited excellent properties for applications in gas sensors, lithium batteries, and photocatalysts due to their large surface area and facile electron (ion) transport. Especially, 3D hierarchical complex architectures assembled by 2D nanostructures have porous structure, present more active sites at large surface area for adsorbing reactant molecules and photocatalytic reactions, thus are desirable for achieving superior photocatalytic activity [27,28]. To date, most of the reported 3D hierarchical Bi_2S_3 architectures are assembled by 1D nanostructure, while there are few reports on the synthesis and photocatalytic performance of 3D hierarchical Bi_2S_3 architectures assembled by 2D nanoplatelets. Therefore, it is essential to design a facile, highly efficient and environmentally friendly route to prepare 3D hierarchical Bi_2S_3 architectures assembled by 2D nanoplatelets for improving visible-light photocatalyitic activity.

Hydrothermal synthesis technique, an effectively and simply controlled solution-based method, involves the formation of well-crystallized products at relatively low temperatures, which has been widely adopted for the synthesis of nanostructured photocatalysts with tailored morphologies [29–31]. In this study, we reported a facile hydrothermal synthesis route for preparing 3D hierarchical Bi_2S_3 architectures assembled by 2D nanoplatelets. A series of techniques, including XRD, SEM, TEM, nitrogen adsorption–desorption isotherms, and UV-vis diffuse reflectance spectrum (DRS), were used to characterize the as-prepared products. The photocatalytic activities of the as-prepared samples were tested in the degradation of Rhodamine B (RhB) under visible light irradiation.

2. Results and Discussions

2.1. Phase Study

The crystallinity and phase structure of the as-prepared 3D hierarchical Bi_2S_3 architectures were investigated by XRD and Raman spectrum, as displayed in Figure 1. XRD result (Figure 1a) showed that the intensities of the diffraction peaks of the as-prepared Bi_2S_3 samples increased with increasing hydrothermal temperatures, indicating that the degree of crystallinity of the as-prepared Bi_2S_3 samples tended to be strengthened with increasing hydrothermal temperatures. Some other impurity peaks of the as-prepared Bi_2S_3 sample are detected when the hydrothermal temperature is lower than 165 °C. As for the representative Bi_2S_3 sample (BS-2#), all the diffraction peaks can be indexed to be the orthorhombic phase Bi_2S_3 (JCPDS No. 17-0320). No other characteristic peaks are observed, implying that the representative Bi_2S_3 sample (BS-2#) is of high purity. The sharp diffraction peaks of the XRD pattern for the BS-2# sample demonstrate that well-crystallized orthorhombic Bi_2S_3 was successfully achieved under the present synthetic conditions. Interestingly, the intensity ratio of (221) peak to (211) peak seemingly deviates from the standard value, implying that the Bi_2S_3 crystal tends to have special anisotropic growth. Figure 1b shows the Raman spectrum of the BS-2# sample, in which exhibits one sharp peak centered about 130 cm^{-1}, and two mild peaks centered about 400 cm^{-1} and 600 cm^{-1}, respectively. Different morphologies and structures can shift the wavenumbers of Raman spectrum due to the difference in the size and surface photo modes [32,33]; thus, the obtained result of Raman spectrum can also confirm the presence of the orthorhombic phase Bi_2S_3.
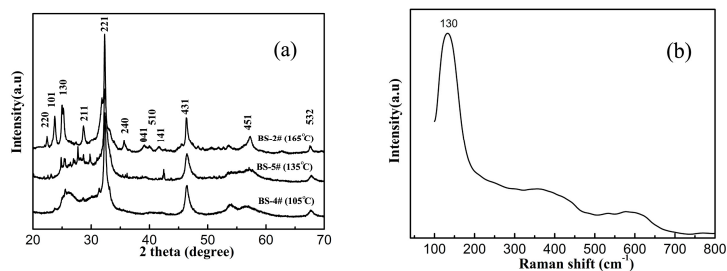
Figure 1. (**a**) XRD patterns of 3D hierarchical Bi_2S_3 architectures prepared at different hydrothermal temperatures; and (**b**) the Raman spectrum of the representative 3D hierarchical Bi_2S_3 architectures (BS-2#).

2.2. Morphology and Proposed Formation Process

Figure 2a shows the low-magnification FESEM image of the representative Bi_2S_3 sample (BS-2#). The BS-2# sample is composed of discrete 3D hierarchical architectures with inhomogeneous size. The higher magnification FESEM image (Figure 2b) reveals that 3D hierarchical architectures has porous structure, in which numerous nanoplatelets are randomly arranged and interconnected. Such a unique structure feature implies that the as-prepared 3D hierarchical Bi_2S_3 architectures are promising to exhibit effective photocatalytic activity for degrading the environmental pollutants. The S- and Bi-mappings of the BS-2# sample are shown in Figure 2d,e, revealing that the BS-2# sample only consists of Bi and S elements. The structure of the BS-2# sample was further investigated by TEM. The result of TEM observation (Figure 3a,b) shows the widths of nanoplatelets are inhomogeneous, while the thickness of nanoplatelets is thin (5–10 nm), which is in good agreement with that of FESEM observation. Figure 3c is a typical HRTEM image taken from the single nanoplatelet, in which an interplanar lattice of 0.374 nm between adjacent lattice fringes can be indexed to (101) plane of orthorhombic phase Bi_2S_3.
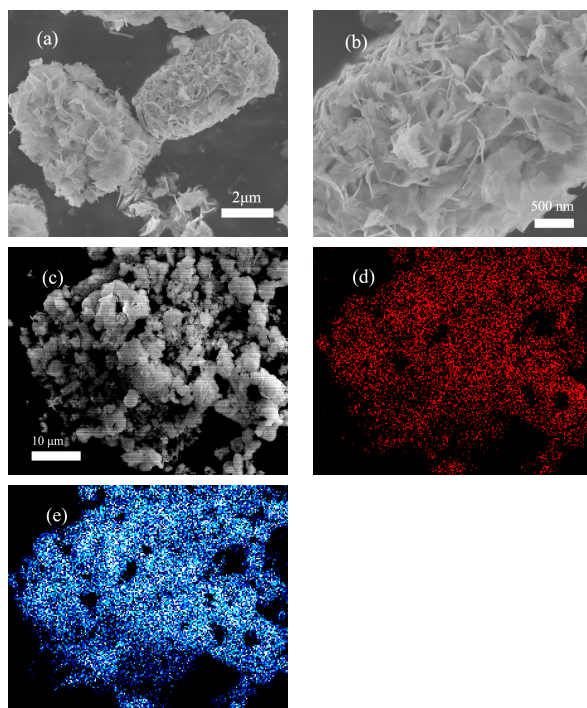

Figure 2. (**a**,**b**) Low magnification and higher magnification FESEM image of the BS-2# sample; (**c**) SEM-EDS elemental mapping of the the BS-2# sample; and the corresponding elemental mappings of (**d**) S and (**e**) Bi.
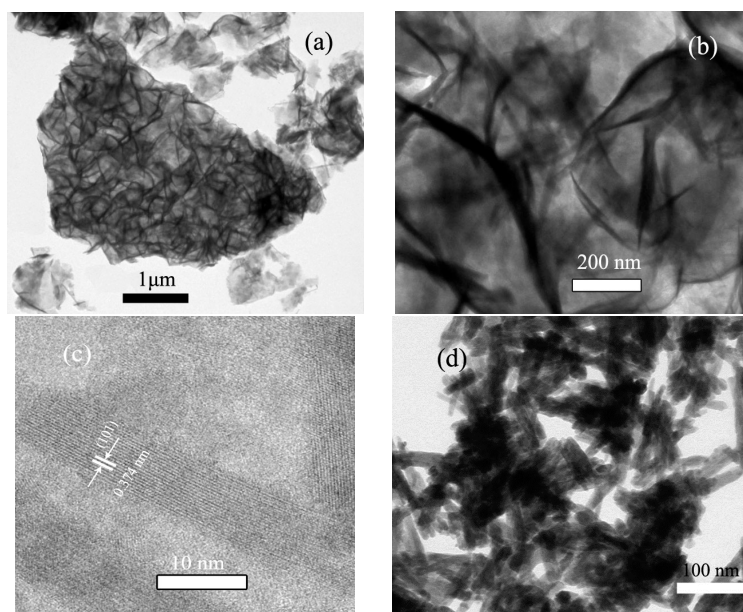
Figure 3. (**a**,**b**) Low-magnification and higher magnification TEM images of the BS-2# sample; (**c**) a typical HRTEM image taken from the single nanoplatelet; and (**d**) TEM image of Bi_2S_3 nanorods.

In order to investigate the effect of the surfactant on the morphology, the hydrothermal synthetic process was carried out without the addition of CTAB. Only Bi_2S_3 nanrods with an average diameter of 20 nm were obtained under such a synthetic condition, as is seen in Figure 3d. Thus, we can infer that the surfactant of CTAB plays a key role in the formation of 3D hierarchical Bi_2S_3 architectures assembled by nanoplatelets. Herein, a probable formation process of 3D hierarchical Bi_2S_3 architectures could be proposed as follows. At initial stage of hydrothermal process, Tu coordinated with Bi^{3+} and formed the Bi^{3+}(III) complexes. Under high pressure and hydrothermal temperature, the Bi^{3+}(III) complexes tended to aggregate and crystal nuclei of Bi_2S_3 came into being in situ. Then, Bi_2S_3 nanoplatelets were formed with the assistance of CTAB. Subsequently, Bi_2S_3 nanoplatelets grew larger and thicker with the ripening process going on. In order to reduce the surface energy, the as-grown Bi_2S_3 nanoplatelets with adsorbed CTAB molecules were likely to convolute and self-assemble loosely, resulting in the formation of 3D hierarchical Bi_2S_3 architectures. The probable formation process is illustrated in Figure 4.
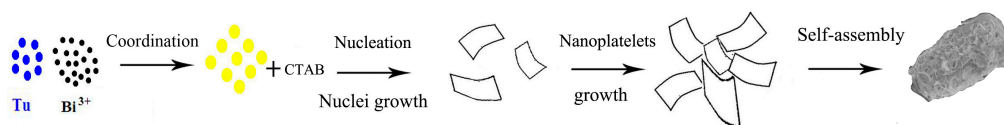

Figure 4. Schematic illustrating the formation process of 3D hierarchical Bi_2S_3 architectures.

2.3. Bet Surface Area and Pore Volume

The specific surface area and pore structure of the BS-2# sample were investigated by nitrogen adsorption–desorption isotherm. Figure 5 depicts the nitrogen adsorption–desorption isotherm and its corresponding pore size distribution of the BS-2# sample. From Figure 5a, we find that the BS-2# sample displays a type IV isotherm with a distinct hysteresis loop in the range of 0.8–1.0 (P/P$_0$), implying the presence of mesopores, which is ascribed to the aggregation of Bi_2S_3 nanoplatelets [34–36]. The specific surface area of the BS-2# sample was calculated to be 49.5 $m^2 \cdot g^{-1}$ by Brunauer–Emmett–Teller equation. Due to its large specific area, the BS-2# sample can absorb more photons and reactants, which results in increasing photocatalytic active sites correspondingly. Moreover, it is clear from Figure 5b that the pore

distribution of t the BS-2# sample exhibits two kinds of mesopores pores with an average diameter of 8.0 nm and 38.3 nm. Based on above results, the obtained mesoporous structure of photocatalyst provides efficient transport pathways to the interior, which may be extremely useful for improving its photocatalytic activity.
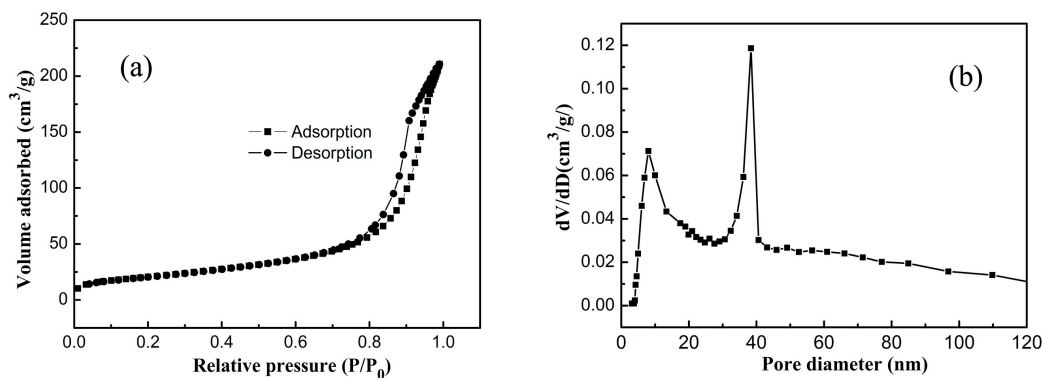

Figure 5. (**a**) Nitrogen adsorption–desorption isotherm; and (**b**) the corresponding pore size distribution of the BS-2# sample.

2.4. Uv-Vis Spectra

As is well known, the photocatalytic activities of photocatalysts are strongly dependent on their energy band structure. Thus, UV-vis diffuse reflectance spectrum (Figure 6) was recorded to obtain optical properties of the BS-2# sample. It is clearly seen from Figure 6a that the BS-2# sample displays good optical absorption ability in the entire visible light region. Consulting the previous studies [37], the band gap (Eg) of Bi_2S_3 can be explored by the extrapolation method based on Kubelka–Munk equation. The above equation can be expressed as $A(h\nu-E_g)^2 = (\alpha h\nu)$, where α is the adsorption coefficient, A is the constant, $h\nu$ is the photon energy, n = 2 for an indirectly allowed transition semiconductor and n = 1/2 for directly allowed transition semiconductor. Figure 6b plots the $(\alpha h\nu)^2$ against photo energy ($h\nu$) curve. The band gap energy of the BS-2# sample is estimated to be 1.48 eV, which is approximate to the reported band gap energy [32,38]. Based on the results, the as-obtained 3D hierarchical Bi_2S_3 architectures belong to one kind of relatively narrow band-gap semiconductors, indicating that more optical energy could be utilized to produce photo-generated carriers for taking part in the photocatalytic degradation reaction.
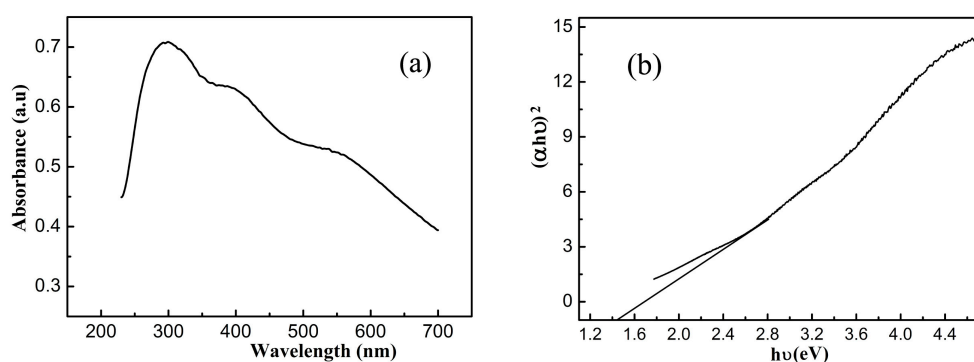

Figure 6. (**a**) UV-vis diffuse reflectance spectrum of the BS-2# sample; and (**b**) the corresponding $(\alpha h\nu)^2$ vs. photon energy ($h\nu$) plots of the BS-2# sample.

2.5. Photocatalytic Activities

The photocatalytic activity of the as-prepared Bi_2S_3 samples was evaluated by degrading RhB aqueous solution under visible light irradiation. The changes in the absorption spectra of RhB at 554 nm were used to monitor the photocatalytic performance. It is well established that synthetic conditions of photocatalysts are likely to affect the crystallinity and shape of the as-prepared samples. Thus, we compared the photodegradation of 3D hierarchical Bi_2S_3 architectures obtained under different hydrothermal temperature, time and pH value in this work. As is shown in Figure 7a, no obvious variation of RhB concentration was observed in the absence of either photocatalyst or light irradiation. Only 6% RhB can be degraded by pure TiO_2 (P25) after irradiating for 60 min. The degradation rate of the BS-2# sample reaches 98.6% after irradiating for 80 min under visible light, while 72.3% and 74.9% degradation rates of RhB are observed for BS-1# and BS-3# sample, respectively. It can also be seen from Figure 7b that the BS-2# sample has the highest photocatalytic efficiency, while 70.5% and 90.1% degradation rates of RhB are observed for BS-4# and BS-5# sample, respectively. Figure 7c shows that the degradation rate of RhB over the as-prepared 3D hierarchical Bi_2S_3 architectures increased with increasing pH value, then decreased. Thus, the factors of temperature, time and pH value exert a significant effect on the photocatalytic efficiency of the as-prepared 3D hierarchical Bi_2S_3 architectures. The explanation can be summarized as follows. The crystallinity and crystalline size vary with the changes of hydrothermal temperature, time and pH value, implying that crystal defects and bandgaps will change correspondingly. The improvement of crystallinity implies that crystal defects acting as photogenerated electron–hole recombination centers will decrease in photocatalysts, while the spectral absorption ability will weaken with increasing crystalline size. Thus, the variation of photocatalytic efficiency of photocatalysts is mainly ascribed to the synergistic effect of the crystallinity and crystalline size. As is shown in Figure 7d, the degradation efficiency of the as-prepared Bi_2S_3 nanorods is only 63.1%. Obviously, the BS-2# sample exhibits much better photocatalytic activity than Bi_2S_3 nanorods. Figure 8 shows the variations of absorption spectra of RhB aqueous solution in the presence of the BS-2# sample and Bi_2S_3 nanorods. It can be found from Figure 8 that the intensity of the characteristic absorption peak of RhB decreased with the irradiation time prolonging. Meanwhile, the color of the suspension faded away gradually during the degradation process. The RhB aqueous solution was almost degraded by the BS-2# photocatalyst after irradiating for 80 min, while the photocatalytic activity of Bi_2S_3 nanorods was more inferior to that of the BS-2# photocatalyst.

It is generally accepted that photocatalytic activities are strongly dependent on the structural features of photocatalysts [39,40]. In this work, ultra thin Bi_2S_3 nanoplatelets can provide large specific surface area, which leads to enhanced absorption and light harvesting. In addition, nanoplatelets with ultra thickness will accelerate the transfer rate of photo-generated carriers from the inside to the surface of the crystal, in which they react with the organic molecules. Thus, the ultrathin structure facilitates the prompt separation of the photo-generated electron–hole, and the probability of the photo-generated electron–hole pairs will be reduced in turn. Base on the above demonstration, 3D hierarchical Bi_2S_3 architectures have porous structure, provide more active sites at large surface area for adsorbing reactant molecules and photocatalytic reactions, and present enhanced photo-generated electron–hole separation rate [7,27,28]. Accordingly, the representative 3D hierarchical Bi_2S_3 architectures exhibits higher photocatalytic efficiency, revealing that the photocatalytic activity of 3D hierarchical Bi_2S_3 architectures are strongly related to the factors of crystallinity, shape and surface area, and the effects of these factors on the photoactivity are interdependent.
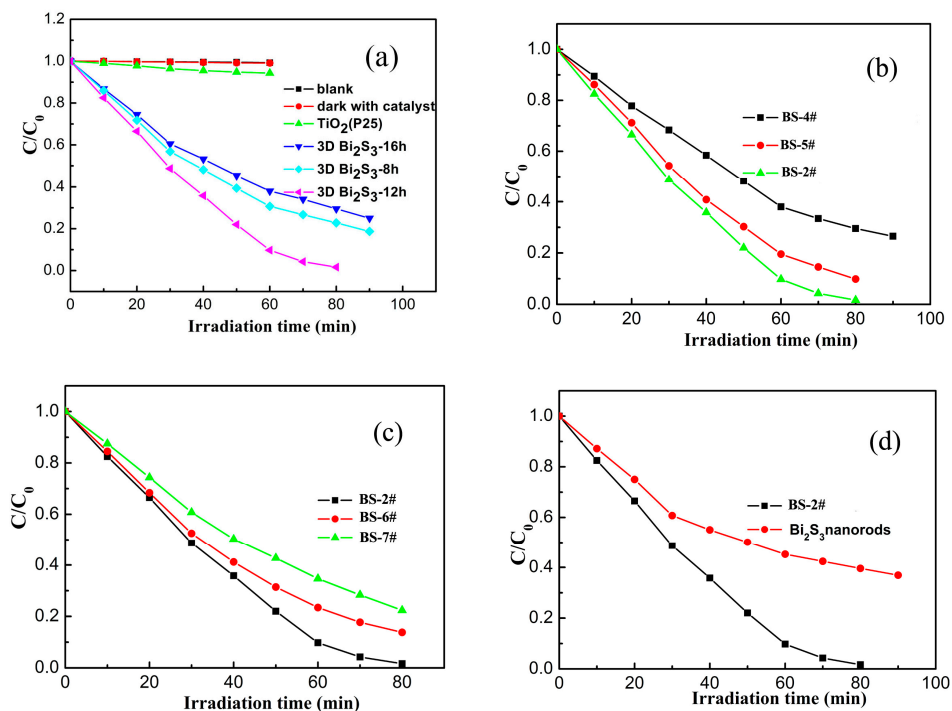
Figure 7. (**a**) The photocatalytic activities of RhB solution in the dark, without catalyst and over the samples of P25, BS-1#, BS-2# and BS-3#; (**b**) the comparison of photocatalytic activity over the samples of BS-2#, BS-4# and BS-5#; (**c**) the comparison of photocatalytic activity of over the samples of BS-2#, BS-6# and BS-7#; and (**d**) the comparison of photocatalytic activity over the samples of BS-2# and Bi_2S_3 nanorods.
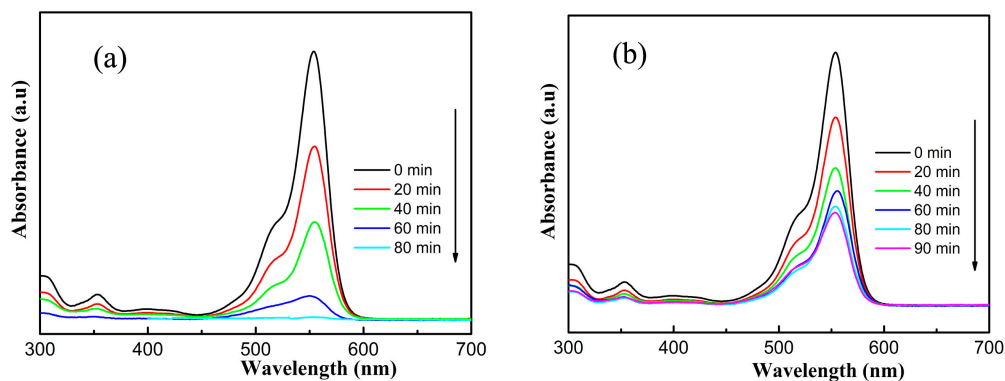

Figure 8. The variations of adsorption spectra of aqueous RhB over different phototocatalysts: (**a**) the BS-2# sample; and (**b**) Bi_2S_3 nanorods.

To make the photodegradation reaction clear, ammonium oxalate (AO), methanol (ME), and benzoquinone (BQ) were used as scavenges of active holes (h^+), hydroxyl radicals ($\bullet OH$), and superoxide radicals ($\bullet O_2^-$) to investigate the effects of reactive species on the photodegradation process of RhB solution [41]. As shown in Figure 9, both AO and BQ cause a strong suppression on the photodegradation process of RhB solution while ME exhibited a relatively weak effect. The above results reveals that the reactive species of h^+ and $\bullet O_2^-$ played a more significant role than $\bullet OH$ for the photodegradation of RhB, which is similar to the previous studies [42,43]. Because the stability has always been a critical concern for an excellent photocatalyst, it is essential to investigate the stability and repeatability of 3D hierarchical Bi_2S_3 architectures in the photodegradation of RhB solution. Thus, the BS-2# sample was recycled for five times under the same conditions, and the corresponding results

are shown in Figure 10. The photocatalytic activity of the BS-2# sample exhibits no significant loss after five cycling runs of photodegradation of RhB, indicating that the BS-2# sample is an efficient visible-light-driven photocatalyst, good reusability and stability for potential practical application in wastewater treatment.
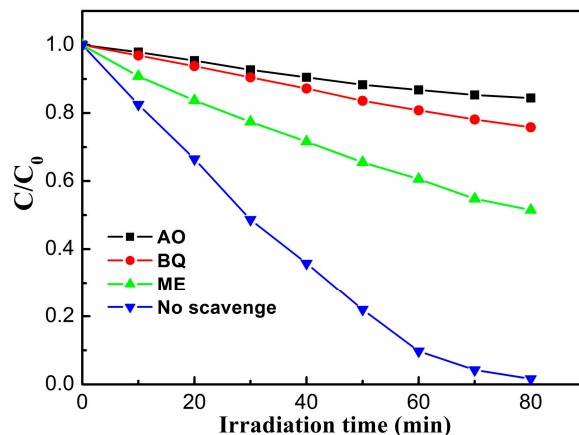

Figure 9. The effects of reactive species involved in the photodegradation of RhB solution over the BS-2# sample.
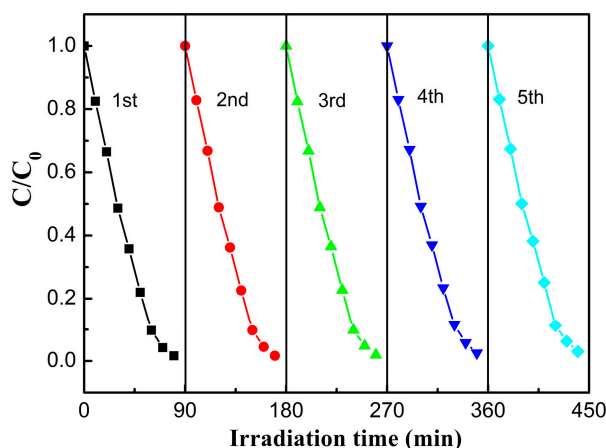

Figure 10. Cycling performance of the photodegradation of RhB solution over the BS-2# sample.

3. Experimental Section

3.1. Synthesis of 3D Hierarchical Bi_2S_3 Architectures

All the reagents obtained from Shanghai chemical industrial Co. Ltd. China were analytically pure and used without any further purification. In a typical synthesis procedure, 2 mmol of bismuth nitrate pentahydrate ($Bi(NO_3)_3 \cdot 5H_2O$) were dissolved in 20 mL mixture solution under vigorous stirring, which consisted of deionized water (8 mL) and dilute nitric acid (1M 12 mL). Then, 0.2 mmol of cetyltrimethyl ammonium bromide (CTAB) was added into the above solution. Next, 3 mmol of thioacetamide (Tu) was dissolved into 40 mL deionized water under stirring to form a homogeneous solution. After that, the Tu solution was slowly dropped into the above bismuth nitrate solution under constant magnetic stirring at room temperature. Subsequently, the pH value of the mixing solution was adjusted to be a certain value. After 1 h, the resulting mixture solution was transferred to Teflon-line stainless steel autoclave with 100 mL capacity and held at different temperatures for a certain time. After the autoclave was cooled naturally to room temperature, the final black precipitates were centrifuged and washed with deionized water and alcohol, respectively, followed by drying

at 60 °C for 10 h in a vacuum oven. The detailed experimental conditions for the preparation of 3D hierarchical Bi_2S_3 architectures are listed in Table 1. As a comparison, Bi_2S_3 nanorods were also prepared by reacting $Bi(NO_3)_3$ and Tu without CTAB.

Table 1. Summary of 3D hierarchical Bi_2S_3 architectures experimental conditions.

Sample	Temperature (°C)	Reaction time (h)	pH value
BS-1#	165	8	2.4
BS-2#	165	12	2.4
BS-3#	165	16	2.4
BS-4#	105	12	2.4
BS-5#	135	12	2.4
BS-6#	165	12	1.0
BS-7#	165	12	4.0

3.2. Characterization

Powder X-ray diffraction (XRD) measurements of the as-prepared 3D hierarchical Bi_2S_3 architectures were carried out with a Bruker AXS D8 Advance diffractometer with Cu Kα radiation (λ = 0.15406nm) over a range from 10° to 70° (Bruker, Billerica, MA ,USA). Surface morphology was observed by using a Hitachi S-4800 (Hitachi, Toyko, Japan) field emission scanning electron microscope. Transmission electron microscopy (TEM) was obtained by using a JEM-2100 microscope (JEOL Ltd., Tokyo, Japan). The Brunauer–Emmett–Teller (BET) surface area was determined on the basis of nitrogen adsorption and desorption isotherms at 77 K using a Quantachrome NOVA 2000e sorption analyzer (Quantachrome Instruments, Boynton Beach, FL, USA). Raman spectrum were carried out by using a Renishaw invia spectrometer (Renishaw, London, UK) at room temperature, and the excitation source was an Ar^+ laser with 514 nm line. UV-vis diffuse reflectance spectrum was collected from a UV-vis spectrophotometer (TU 1901, Puxi, Beijing, China) with $BaSO_4$ as reference.

3.3. Photocatalytic Activity

The photocatalytic activities of the as-prepared Bi_2S_3 samples were evaluated by the degradation of RhB aqueous solution under visible-light irradiation. As was reported in our previous work [29–31], 40 mL RhB aqueous solution with a concentration of 1.0×10^{-5} M was added into the culture dish with 0.05 g prepared photocatalyst. A 30 W fluorescent lamp was used as light source to trigger the photocatalytic reaction, and the distance between the lamp and the dish coated by the photocatalysts was about 10 cm. Prior to irradiation, an adsorption–desorption equilibrium was demanded to reach among the catalyst, RhB and water in the dark. At given time intervals, 5 mL of the reacted solution was centrifuged for concentration analysis. The concentration of RhB aqueous solution was determined by recording the variation of the intensity of absorption peak located at 554 nm using an UV-visible spectrophotometer (TU1901, Puxi, Beijing, China). The photo-degradation efficiency of RhB was evaluated by $(C_0-C)/C_0$, where C is the concentration of the RhB solution at reaction time t, C_0 is the adsorption/desorption equilibrium concentration of RhB (at reaction time 0).

4. Conclusions

In summary, we demonstrated a facile hydrothermal route for preparing 3D hierarchical Bi_2S_3 architectures. The as-prepared 3D hierarchical Bi_2S_3 architectures in which abundant nanoplatelets are randomly arranged and interconnected with each other have porous structure and large specific surface area. The formation process of 3D hierarchical Bi_2S_3 architectures was proposed. The enhanced photocatalytic activity of the representative 3D hierarchical Bi_2S_3 architectures could be ascribed to the synergetic effect of the shape, surface area, crystallinity, band gap and crystalline size. Considering the facile synthesis method and superior photocatalytic activity, the as-prepared 3D hierarchical Bi_2S_3

architectures are promising to speed up the application of visible-light photocatalysts in the field of environmental remediation.

Author Contributions: Tiekun Jia conceived and designed the experiments; Jili Li and Zhihua Kang performed the synthetic experiment; Xiaofeng Wang and Fei Long analyzed the data; Guang Sun gave basic and important ideas as well as precise instruction; Fang Fu and Jian Chen performed the photo-catalytic activity of the as-prepared samples; and Tiekun Jia wrote the paper.

Conflicts of Interest: The authors declare no conflict of interest.

Abbreviations

The following abbreviations are used in this manuscript:

XRD	X-ray diffraction
SEM	Scanning electron microscopy
TEM	Transmission electron microscopy
HRTEM	High resolution transmission electron microscopy
BET	Brunauer-Emmett-Teller
DRS	Diffuse reflectance spectrum
1D	One dimensional
2D	Two-dimensional
3D	Three-dimensional
RhB	Rhodamine B
CTAB	Cetyltrimethyl ammonium bromide
BET	Brunauer-Emmett-Teller
DRS	Diffuse reflectance spectrum

References

1. Zou, Z.G.; Ye, J.H.; Sayama, K.; Arakawa, H. Direct splitting of water under visible light irradiation with an oxide semiconductor photocatalyst. *Nature* **2001**, *414*, 625–627. [CrossRef] [PubMed]

2. Hernandez-Alonso, M.D.; Fresno, F.; Suarez, S.; Cornnado, J.M. Development of alternative photocatalysts to TiO_2: Challenges and opportunities. *Energy Environ. Sci.* **2009**, *2*, 1231–1257. [CrossRef]

3. Zhang, Z.G.; Huang, Z.F.; Cheng, X.D.; Wang, Q.L.; Chen, Y.; Dong, P.M.; Zhang, X.W. Product selectivity of visible-light photocatalytic reduction of carbon dioxide using titanium dioxide doped by different nitrogen-sources. *Appl. Sur. Sci.* **2015**, *355*, 45–51. [CrossRef]

4. Tu, W.G.; Zhou, Y.; Zou, Z.G. Photocatalytic conversion of CO_2 into renewable hydrocarbon rules: State-of-the-art accomplishment, challenges, and prospects. *Adv. Mater.* **2014**, *26*, 4607–4626. [CrossRef] [PubMed]

5. Truong, Q.D.; Le, T.H.; Liu, J.Y.; Chung, C.C.; Ling, Y.C. Synthesis of TiO_2 nanoparticles using novel titanium oxalate complex towards visible light-driven photocatalytic reduction of CO_2 to CH_3OH. *Appl. Cata. A Gen.* **2012**, *437*, 28–35. [CrossRef]

6. Paola, A.D.; Bellardita, M.; Palmisano, L. Brookite, the least known TiO_2 photocatalyst. *Catalysts* **2013**, *3*, 36–73. [CrossRef]

7. Liu, B.S.; Nakata, K.; Sakai, M.; Saito, M.; Ochiai, T.; Murakami, T.; Takagi, K.; Fujishima, A. Hierarchical TiO_2 spherical nanostructures with tunable pore size, pore volume, and specific surface area: Facile preparation and high-photocatalytic performance. *Catal. Sci. Technol.* **2012**, *2*, 1933–1939. [CrossRef]

8. Rath, A.K.; Bernechea, M.; Martinez, L.; Konstantatos, G. Solution-processed heterojunction solar cells based on *p*-type PbS quantum dots and *n*-type Bi_2S_3 nanocrystals. *Adv. Mater.* **2011**, *23*, 3712–3717. [CrossRef] [PubMed]

9. Zhang, H.; Yang, L.; Liu, Z.; Ge, M.; Zhou, Z.; Chen, W.; Li, Q.; Liu, L. Facet-dependent activity of bismuth sulfide as low-cost counter-electrode materials for dye-sensitized solar cells. *J. Mater. Chem.* **2012**, *22*, 18572–18577. [CrossRef]

10. Li, Y.P.; Wei, F.; Ma, Y.G.; Zhang, H.; Gao, Z.W.; Dai, L.; Qin, G.G. Selected-control hydrothermal synthesis and photoresponse properties of Bi_2S_3 micro/nanocrystals. *CryEngComm* **2013**, *15*, 6611–6616. [CrossRef]

11. Li, R.; Yang, J.; Fan, C.; Lu, F.; Wei, Z.; Li, J. Effect of electrical contact on the performance of Bi_2S_3 nanowire photodetectors. *ChemPhysChem* **2014**, *15*, 2510–2516. [CrossRef] [PubMed]

12. Chen, G.H.; Yu, Y.Q.; Zheng, K.; Ding, T.; Wang, W.L.; Jiang, Y.; Yang, Q. Fabrication of ultrathin Bi_2S_3 nanosheets for high performance, flexible, visible-NIR photodetectors. *Small* **2015**, *11*, 2848–2855. [CrossRef] [PubMed]

13. Xiao, G.J.; Dong, Q.F.; Wang, Y.N.; Sui, Y.M.; Ning, J.J.; Liu, Z.Y.; Tian, W.J.; Liu, B.B.; Zou, G.T.; Zou, B. One-step solution synthesis of bismuth sulfide (Bi_2S_3) with various hierarchical architectures and their photoresponse properties. *RSC Adv.* **2012**, *2*, 234–240. [CrossRef]

14. Li, H.H.; Yang, J.; Zhang, J.Y.; Zhou, M. Facile synthesis of hierarchical Bi_2S_3 nanostructures for photo-detector and gas sensor. *RSC Adv.* **2012**, *2*, 6258–6261. [CrossRef]

15. Schricker, A.D.; Sigman, M.B.; Korgel, B.A. Electrical transport, Meyer-Neldel rule and oxygen sensitivity of Bi_2S_3 nanowire. *Nanotechnology* **2005**, *16*, S508–S513. [CrossRef]

16. Rabin, O.; Perez, J.M.; Grimm, J.; Weissleder, R. An X-ray computed tomography imaging agent based on long-circulating bismuth sulphide nanoparticles. *Nat. Mater.* **2006**, *5*, 118–122. [CrossRef] [PubMed]

17. Ma, J.M.; Liu, Z.F.; Lian, J.B.; Duan, X.C.; Kim, T.; Peng, P.; Liu, X.; Yao, G.; Zheng, W.J. Ionic liquids-assisted synthesis and electrochemical properties of Bi_2S_3 nanostructures. *CrystEngComm* **2011**, *13*, 3072–3079. [CrossRef]

18. Jin, R.C.; Xu, Y.B.; Li, G.H.; Liu, J.S.; Chen, G. Hierarchical chlorophytum-like Bi_2S_3 architectures with high electrochemical performance. *Int. J. Hydroge. Energy* **2013**, *38*, 9137–9144. [CrossRef]

19. Zhang, Z.; Zhou, C.K.; Lu, H.; Jia, M.; Lai, Y.Q.; Li, J. Facile synthesis of dandelion-like Bi_2S_3 microspheres and their electrochemical properties for lithium-ion batteries. *Mater. Lett.* **2013**, *91*, 100–102. [CrossRef]

20. Jung, H.; Park, C.M.; Sohn, H.J. Bismuth sulfide and its carbon nanocomposite for rechargeable lithium-ion batteries. *Electrochim. Acta* **2011**, *56*, 2135–2139. [CrossRef]

21. Vinu, R.; Madras, G. Kinetics of simultaneous photocatalytic degradation of phenolic compounds and reduction of metal ions with nano-TiO_2. *Environ. Sci. Technol.* **2008**, *42*, 913–919. [CrossRef] [PubMed]

22. Cao, J.; Xu, B.Y.; Lin, H.L.; Luo, B.; Chen, S.F. Chemical etching preparation of BiOI/BiOBr heterostructures with enhanced photocatalytic, properties for organic dye removal. *Chem. Eng. J.* **2012**, *185*, 91–99. [CrossRef]

23. Cui, Y.M.; Jia, Q.F.; Li, H.Q.; Han, H.G.; Zhu, L.J.; Li, S.G.; Zou, Y.; Yang, J. Photocatalytic activities of Bi_2S_3/BiOBr nanocomposites synthesized by a facile hydrothermal process. *Appl. Surf. Sci.* **2014**, *290*, 233–239. [CrossRef]

24. Sigman, M.B., Jr.; Korgel, B.A. Solventless synthesis of Bi_2S_3 (bismuthinite) nanorods, nanowires, and nanofabric. *Chem. Mater.* **2005**, *17*, 1655–1660. [CrossRef]

25. Liu, Z.P.; Peng, S.; Xie, Q.; Hu, Z.; Yang, Y.; Zhang, S.; Qian, Y. Large-scale synthesis of ultra long Bi_2S_3 nanoribbons via a solvothermal process. *Adv. Mater.* **2003**, *15*, 936–940. [CrossRef]

26. Zhou, H.Y.; Xiong, S.L.; Wei, L.Z.; Xi, B.J.; Zhu, Y.C.; Qian, Y.T. Acetylacetone-directed controllable synthesis of Bi_2S_3 nanostructures with tunable morphology. *Cryst. Growth Des.* **2009**, *9*, 3862–3867. [CrossRef]

27. Li, G.; Liu, J.; Lan, J.; Li, G.; Chen, Q.; Jiang, G. 3D hierarchical anatase TiO_2 superstructures constructed by "nanobricks" built nanosheets with exposed{001}facets: Facile synthesis, formation mechanism and superior photocatalyticactivity. *CrystEngComm* **2014**, *16*, 10547–10552. [CrossRef]

28. Zhang, H.; Du, G.; Lu, W.; Cheng, L.; Zhu, X.; Jiao, Z. Porous TiO_2 hollow nanospheres: Synthesis, characterization and enhanced photocatalytic properties. *CrystEngComm* **2012**, *14*, 3793–3796. [CrossRef]

29. Jia, T.K.; Wang, W.M.; Long, F.; Fu, Z.Y.; Wang, H.; Zhang, Q.J. Synthesis, characterization, and photocatalytic activity of Zn-doped SnO_2 hierarchical architectures assembled by nanocones. *J. Phys. Chem. C* **2009**, *113*, 9701–9077. [CrossRef]

30. Jia, T.K.; Wang, W.M.; Long, F.; Fu, Z.Y.; Wang, H.; Zhang, Q.J. Fabrication, Characterization and Photocatalytic Activity of La-doped ZnO Nanowires. *J. Alloys Compd.* **2009**, *484*, 410–415. [CrossRef]

31. Jia, T.K.; Fu, F.; Long, F.; Min, Z.Y.; Zhao, J.W.; Chen, J.; Li, J.L. Synthesis, characterization andenhanced visible-light photocatalytic activity of Zn_2SnO_4-C nanocomposites with truncated octahedron morphology. *Ceram. Int.* **2016**, *142*, 13893–13899. [CrossRef]

32. Helal, A.; Harraz, F.A.; Iamail, A.A.; Sami, T.M.; Ibrahim, I.A. Controlled synthesis of bismuth sulfide nanorods by hydrothermal method and their photocatalytic activity. *Mater. Design* **2016**, *102*, 202–212. [CrossRef]

33. Zhang, Y.Y.; Guo, Y.P.; Fang, B.J.; Chen, Y.J.; Duan, H.N.; Li, H. Continuously enhanced photoactivity of hierarchical β–Bi_2O_3/Bi_2S_3 heterostructure derived from novel BiO_2CH_3 octagonal nanoplates. *Appl. Catal. A Gen.* **2016**, *514*, 146–153. [CrossRef]

34. Wang, X.; Li, S.; Yu, H.; Yu, J. In situ anion-exchange synthesis and photocatalytic activity of $Ag_8W_4O_{16}$/AgCl-nanoparticle core-shell nanorods. *J. Mol. Catal. A Chem.* **2011**, *334*, 52–59. [CrossRef]

35. Yuan, Z.Y.; Su, B.L. Surfactant-assisted nanoparticle assembly of mesoporous β-FeOOH (akaganeite). *Chem. Phys. Lett.* **2003**, *381*, 259–267.

36. Ren, T.Z.; Yuan, Z.Y.; Su, B.L. Surfactant-assisted preparation of hollow microspheres of mesoporous TiO_2. *Chem. Phys. Lett.* **2003**, *374*, 170–175. [CrossRef]

37. Butler, M.A. Hotoelectrolysis and physical properties of the semiconducting electrode WO_3. *J. Appl. Phys.* **1977**, *48*, 1914–1920. [CrossRef]

38. Miller, D.D.; Heller, A. Semiconductor liquid junction solar cells based on anodic sulphide films. *Nature* **1976**, *262*, 680–681. [CrossRef]

39. Lu, H.B.; Wang, S.M.; Zhao, L.; Li, J.C.; Dong, B.H.; Xu, Z.X. Hierarchical ZnO microarchitectures assembled by ultrathin nanosheets: Hydrothermal synthesis and enhanced photocatalytic activity. *J. Mater. Chem.* **2011**, *21*, 4228–4234. [CrossRef]

40. Zhang, L.; Yu, J.C. A snochemical approach hierarchical porous titania spheres with enhanced photocatalytic activity. *Chem. Comm.* **2003**, 2078–2079. [CrossRef]

41. Di, J.; Xia, J.X.; Ji, M.X.; Wang, B.; Li, X.W.; Zhang, Q.; Chen, Z.G.; Li, H.M. Nitrogen-doped carbon quantum dots/BiOBr ultrathin nanosheets: In Situ strong coupling and improved molecular oxygen activation ability under visible light irradiation. *ACS Sustain. Chem. Eng.* **2016**, *4*, 136–146. [CrossRef]

42. Cao, J.; Xu, B.Y.; Lin, H.L.; Luo, B.D.; Chen, S.F. Novel Bi_2S_3-sensitized BiOCl with highly visible light photocatalytic activity for the removal of Rhodamine B. *Catal. Comm.* **2012**, *26*, 204–208. [CrossRef]

43. Chen, X.; Li, H.K.; Wu, Y.X.; Wu, H.S.; Wu, L.D.; Tan, P.F.; Pan, J.; Xiong, X. Facile fabrication of novel porous graphitic carbon nitride/copper sulfide nanocomposites with enhanced visible light driven photocatalytic performance. *J. Coll. Inter. Sci.* **2016**, *476*, 132–143. [CrossRef] [PubMed]